The onset of instability in a parametric resonance energy harvester under panchromatic excitations

International Journal of Mechanical Sciences 281 (2024) 109544

Contents lists available at ScienceDirect

International Journal of Mechanical Sciences

journal homepage: www.elsevier.com/locate/ijmecsci

The onset of instability in a parametric resonance energy harvester under panchromatic excitations

Giuseppe Giorgi

Marine Offshore Renewable Energy Lab (MOREnergy Lab), Department of Mechanical and Aerospace Engineering (DIMEAS), Politecnico di Torino, 10129 Torino, Italy

ARTICLE INFO

Keywords:
Parametric resonance
Bezier curves
Wave energy converter
Nonlinear Froude–Krylov force
Panchromatic excitation

ABSTRACT

This paper further explores the potential of parametric resonance to enhance wave energy conversion in a pendulum-based pitching floating energy harvester, considering power extraction and panchromatic excitation. Unlike traditional parametric systems that focus on inertial mechanical instability induced by floater motion, this concept, firstly proposed in a previous recent publication, leverages the parametric resonance induced by nonlinear hydrodynamic coupling between heave and pitch. By deliberately integrating parametric instability into the floater design with a 2:1 ratio of natural periods in two hydrodynamic degrees of freedom, the frequency bandwidth of the mechanical system is expanded, leading to two distinct regions of significant power production. The research advances current understanding in three key areas: (i) the use of Bezier curves to advance a computationally efficient nonlinear hydrodynamic model based on nonlinear Froude–Krylov force calculations tailored for prismatic floaters, (ii) investigation of the impact of power extraction on the severity of nonlinear parametric resonance, and (iii) consideration of more realistic panchromatic waves to quantify the onset of instability and the decrease in the severity of parametric resonance response, also addressing practical implications for numerical simulations and signal processing. Findings indicate that beneficial parametric resonance persists across various damping and wave conditions, although the relative importance of the contribution of the 2:1 parametric resonance region to power extraction decreases by 75%, on average.

1. Introduction

The field of wave energy conversion is currently living at a tipping point [1]: on the one hand, the extremely high potential of production of renewable energy exploiting ocean waves is broadly recognized, not only by the academia [2], but also by policy-makers [3] and funding agencies [4], thanks to its complementarity with other renewable energy sources [5] and widespread availability [6]; on the other hand, ambitions are yet to be met, as the industry is still struggling to reduce the livelised cost of energy (LCoE) to become competitive with other renewable energy sources [7]. Techno–economic optimizations based on representative continuously improving estimations of LCoE [8] are the main routes followed to achieve economic viability. In addition, in the pursue of increasing the energy conversion effectiveness, the classic ocean engineering field is opening up to new mechanical systems to develop novel working principles, trying to overcome inherent limitations of more mature concepts: for example, Zheng et al. [9] propose a variable aperture point absorber, while Olbert and Abdel-Maksoud [10] leverage lift-based systems instead of the more conventional pressure-based devices. In both cases, numerical models are at the cornerstone and success strictly depends on their effectiveness.

The discussion on numerical models and signal processing for wave energy applications unfolds according to two main aspects, i.e. fidelity and computational time, which are normally antagonistic: higher accuracy is often achieved by including nonlinearities into the mathematical model, typically making it slower to compute. Such an interplay is compromised by the requirements of the specific application the model is needed for: optimizations demand for low computational time and can cope with lower accuracy, while survivability assessments urge for the highest fidelity being keen to withstand higher computational burden. Hybrid attempts to exploit the pros of both approaches are data-driven techniques [11], which identify a lean structure based on a higher-fidelity model [12].

Within this context, wave energy converters may show some specific nonlinear dynamics with relevant engineering applications, such that the choice of the appropriate numerical model and signal processing technique is paramount. In wave–structure interactions for wave energy converters (WECs), the development of nonlinear vibrations and their effect on the simulated results are related to specific physical phenomena; for the sake of discussion, their accuracy can be classified as either

E-mail address: giuseppe.giorgi@polito.it.

https://doi.org/10.1016/j.ijmecsci.2024.109544
Received 21 April 2024; Received in revised form 13 June 2024; Accepted 3 July 2024
Available online 10 July 2024

incremental or *Boolean*. An example of incremental accuracy is related to viscous drag: linear potential flow models either neglect viscosity, or include corrective linearized viscous coefficients [13] or Morison elements [14]; finally, fully nonlinear models better include viscosity via Navier–Stokes equations in Computational Fluid Dynamics (CFD) [15] or Smoothed Particle Hydrodynamics (SPH) [16]. As a consequence, accuracy is expected to *gradually increase* as the complexity of the model (and its computational time) increases.

Differently from incremental nonlinear fidelity, Boolean accuracy herein refers to highly nonlinear dynamics that are completely overlooked by linear or linearized models. Especially telling examples of these phenomena are Vortex Induced Vibrations (VIV) [17], likely requiring CFD simulations [18], and parametric resonance [19]: both are overseen by linear or partially non-linear models, and both can have either positive or detrimental effects in engineering applications. Indeed, hydrodynamic models used for mechanical systems design and concept development are often simplified, especially for fluid–structure interactions, due to the strict requirement on computational time [20]; therefore, if strong nonlinear dynamics arise, they are often unexpected and, consequently, likely to be detrimental. VIV has been found as an unexpected source of nonlinear vibration of mooring lines, potentially threatening fatigue resistance [21]; similarly, parametric resonance typically decreases the power conversion efficiency of wave energy converters [22]. Conversely, if appropriate numerical models are used at the design stage, the same nonlinear vibration phenomena can be leveraged to improve, or even enable, the power conversion: to date, VIV is already commonly used as the primary excitation mechanism for some energy harvesters [23], reaching a discrete maturity with air-foil based piezoelectric systems [24].

Nonlinearities are often included into the dynamical system to enlarge the energy conversion bandwidth [25]: examples include hardening stiffness in piezoelectric harvesters [26], 1:2 internal resonance in cantilever VEHs [27], stoppers [28], parametric oscillators [29], bi-stability [30], or snap-through mechanisms [31]. Vibration energy harvesters typically embed internal resonance into their design to broaden the frequency bandwidth and perform well also at lower frequencies than the linear resonance [32], and to be responsive al lower excitation thresholds [33]. Wave energy applications, much of the work exploiting nonlinear mechanisms to enhance performance has been focused on point absorbers (PA) [34]: the intentional incorporation of a nonlinear restoring force has been borrowed from the field of vibratory energy harvesting [35], where nonlinearity is used to broaden the bandwidth of vibration harvesters, which encounter similar performance challenges as linear point absorbers (PAs). One initial approach involves introducing a bi-stable restoring force into the PA dynamics [36], using conventional [37] or adaptive [38] bi-stable mechanisms, pneumatic [39] or magnetic [40]. Alternatively, some mechanisms have been proposed that are capable of exhibiting not only bi-stable behaviour but also tri-stable and quad-stable behaviours [41]. Mechanical springs have the practical issue of occupying significant space; to avoid this, magnetic mechanisms have been proposed to introduce bi-stability into the design of the converter [42]. Other attempts include the use of a vibro-impact mechanism or end stoppers [43] and shock mechanisms [44], inside an inertial buoy [45] or the power take-off [28], to create a nonlinear hardening response with a quasi-linear dependence of the restoring force on the buoy motion.

Parametric resonance is commonly present in the literature for energy harvesting, particularly within the common embodiment of the parametric pendulum, which has also been applied in the wave energy conversion field [46]; here, the effort has been focused on making the embodiment technically viable, for example by means of multiple pendulums [47], eventually to be synchronized [48], bifurcation control [49], or sloped geometrical configuration to decrease the effective influence of gravity [50]. Other sparse examples of leveraging nonlinearities in ocean energy include the use of negative stiffness mechanisms, for example used for a hinged device in [51] and a raft-type device in [52]. In the field of wave energy, parametric resonance has been observed in various floating systems, such as tethered bodies and self-referenced two-body configurations. Examples include offshore floating oscillating water columns [53], floating sloped devices [54], pendulum-based WECs [55], two-body self-referenced WECs [56], and bottom-tethered systems [57]. In these instances, parametric resonance can decrease energy conversion efficiency by diverting energy away from the degree of freedom equipped with the PTO system, thereby reducing the available energy. Additionally, it can impose higher and unexpected loads on other WEC subsystems, particularly the mooring system, potentially causing damage and lowering reliability. To address the challenges posed by parametric instability, specific detection and suppression strategies are employed to mitigate its effects. However, when intentionally incorporated into the design or actively triggered, it can actually bring benefits to the performance of the system. To date, examples in the wave energy field are rare, since modelling parametric resonance at the early stages of design is challenging, due to computational constraints. However, it is worth mentioning instances in floating [58] or onshore [59] oscillating water columns, as well as attenuators [60].

Recently, a novel working principle has been proposed for improving the wave energy conversion in a pitching device [61]. It is worth noting that parametric pendula, well-known in the literature, exploit the heaving motion to harvest energy; conversely, the proposed concept extracts energy from the pitching motion of the floater, whose range can be increased thanks to parametric resonance and nonlinear hydrodynamic coupling between heave and pitch. Indeed, the novel design purposely embeds parametric resonance in a notional floater, in order to enlarge the frequency bandwidth of the mechanical system. Thanks to a 2:1 ratio of the natural frequencies in heave and pitch, parametric instability is triggered within the operational range of the system; this entails the presence of two regions of significant power production, instead of the single region predicted by linear models. [61] has proposed the proof of concept, demonstrating and quantifying the higher mechanical energy availability at the shaft of the power take-off (PTO); however, [61] is limited to undamped oscillations subject to monochromatic wave excitations. Conversely, this paper advances the state-of-the-art via the following three major novelties:

(i) Novel and more general description of the nonlinear hydrodynamic model, based on computationally efficient nonlinear Froude–Krylov force (NLFK) calculation for prismatic floaters: the novelty is the use of a single Bezier curve of arbitrary complexity to define the shape of the prismatic floaters, while the latest algebraic description available in the literature uses multiple portions of circumferences [62];
(ii) Having a more effective NLFK model, this paper investigates the effect of power extraction on the severity of the nonlinear parametric resonance response, still considering monochromatic excitations: the research question is whether the damping effect of the PTO system neutralizes the positive effect of the induced nonlinear vibration, or if the nonlinear response remains relevant for the power extraction objective;
(iii) Finally, more realistic panchromatic waves are considered: since parametric resonance is highly sensitive to the frequency content of the exciting signal, this papers investigates more realistic triggering effects leading to the onset of instability and quantifies the further decrease in the severity of parametric resonance response. The signal processing of the simulated panchromatic nonlinear vibration response is discussed, delving into the practical consequences of stochastic variability, length of the signal, and significance of the instantaneous frequency and its variability within the signal generated from realistic ocean wave spectra.

The remainder of the paper is organized as follows: Section 2 introduces the mechanical system subject of this paper, briefly presenting the underlying parametric resonance phenomenon in Section 2.1, the mechanical working principle of the wave energy converter in Section 2.2, and finally the time-domain numerical model to simulate the nonlinear responses to various types of forcing input signals (up- and down-chirps, monochromatic and panchromatic waves) in Section 2.3. Section 3 describes the computationally efficient nonlinear wave–structure interaction solver, based on a Bezier-curve compact description. Finally, Section 4 presents results, with and without power extraction, considering monochromatic and panchromatic waves, in Sections 4.1 and 4.2, respectively. Section 5 draws concluding remarks and summarizes the major findings of the paper.

2. The mechanical system: A 2:1 parametric resonance wave energy converter

The mechanical system herein proposed is a wave energy converter purposely designed to experience parametric resonance such that the mechanical energy available at the PTO shaft is increased over a broader range of frequencies. To discuss this beneficial effect, parametric resonance is first generally introduced in Section 2.1, then embedded within a working principle for a WEC in Section 2.2.

2.1. Parametric resonance

Time-fluctuations of one or more parameters of a system can lead to parametric resonance, i.e. a nonlinear process that triggers internal excitation [63]. In the field of nonlinear dynamics, it is common to use a Mathieu-type instability to initially explain this occurrence. Considering a simplified and idealized equivalent mechanical system, parametric instability in the Mathieu form is represented by a second-order differential equation for a single degree of freedom (DoF) system, involving a generic variable χ. The equation includes a time-varying stiffness component that follows a harmonic function with a circular frequency ω_c; then, in practical engineering scenarios, the damped Mathieu equation is often employed:

$$\ddot{\chi} + \mu\dot{\chi} + (\Delta + \Lambda\cos\tau)\,\chi = 0, \tag{1}$$

where derivations in time are performed with respect to the dimensionless $\tau = \omega_c t$, Δ is a dimensionless stiffness, Λ is the corresponding dimensionless amplitude of the stiffness oscillation, and μ is a dimensionless dissipative coefficient. It is possible to derive the stability diagram of Eq. (1), represented in Fig. 1, where ω_n is the natural frequency of the 1-DoF system and $\Delta^2 = \omega_n/\omega_c$; in such an idealized case, two triggering condition for the onset of instability exist (coloured areas in Fig. 1): (i) the exciting frequency is double of or equal to the internal frequency ($\Delta = 0.25$ or $\Delta = 1$, respectively), and (ii) the excitation amplitude (Λ) is sufficiently large to overcome the internal dissipation (μ).

The objective of this paper is to investigate and quantify how these two idealized triggering conditions for a simple 1-DoF harmonic oscillator, as well as the intensity of the parametric resonance response, change for a multi-DoF wave energy converter, subject to energy extraction (which effectively acts as an additional dissipation mechanism) and realistic panchromatic excitations.

2.2. 2:1 WEC working principle

As mentioned in Section 2.1, parametric resonance is due to time-varying parameters; in floating systems immersed in a wave field, such time-variations are mostly due to the relative motion between the exciting waves and the instantaneous position of the displaced body. This causes a nonlinear coupling between heaving and pitching motions, which would be linearly uncoupled otherwise. This nonlinear coupling between heave and pitch is mainly due to the influence of

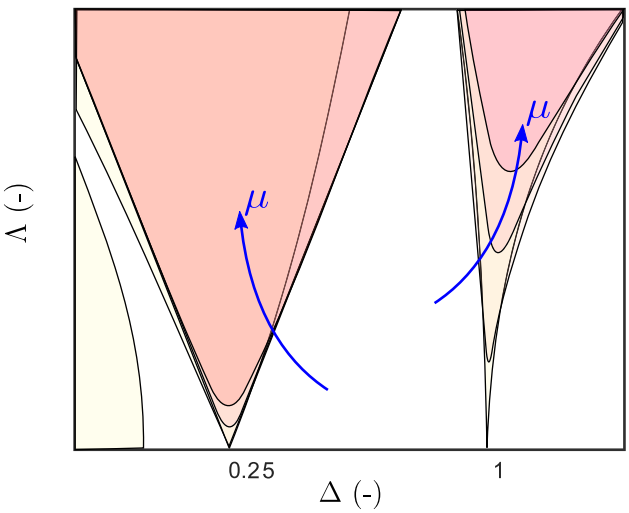

Fig. 1. Stability diagram of the damped Mathieu equations (1). The shaded regions refer to instability: they appear when the exciting frequency is double of or equal to the internal frequency ($\Delta = 0.25$ or $\Delta = 1$, respectively), and for excitation amplitude (Λ) sufficiently large to overcome the internal dissipation (μ).

heave motions on the pitch restoring term, which is notionally (to a first approximation) dependent on two parameters [64]: the submerged volume (∇) and the metacentric height ($\overline{GM}$), which change as the instantaneous wetted surface changes during the motion of the system [65]. In addition, since the NLFK model herein implemented considers both the static and dynamic Froude–Krylov forces, the nonlinear coupling is more complex and less transparent than the first approximation related to just the ∇ and $\overline{GM}$; nevertheless, the underlying cause of the coupling remains the time variations of the wetted surface, which eventually becomes not symmetric, hence with nonlinear coupling between otherwise uncoupled degrees of freedom. Therefore, once parametric resonance is triggered, there is an open channel to transfer part of the mechanical energy between such degrees of freedom, due to the hydrodynamic nonlinear coupling, akin to vibrational energy transfer in coupled mechanical systems with nonlinearities [66].

Parametric resonance is detrimental for energy conversion applications if this nonlinear coupling diverts part of the incoming energy *away* from the DoF where the PTO is installed [67]. Conversely, it can be an enabling additional excitation mechanism if purposely exploited to transfer more energy to the PTO shaft, as proposed in [61]. The system, schematically presented in Fig. 2, is devised as follows: a pendulum is contained within a sealed hull, such that the pitching motion of the floater mostly entails an inertially-activated rotation of the pendulum about its pivot hinge, where a PTO is installed to extract power. Experimental implementations and validation of similar systems are available in the literature [68]. However, without parametric resonance, such a system is effective only when the frequency of the incoming wave is about the same of the pitching natural frequency. Conversely, Giorgi [61] proposes to design a system prone to parametric resonance, such that it leads to a second region of significant energy extraction.

The notional design of the system is based on both the simplified triggering condition from the Mathieu equation (excitation frequency is equal or twice the natural period in the pitch DoF), and the nonlinear hydrodynamic coupling between the pitch and heave DoFs. Thus, the WEC is designed to have a 2:1 ratio between the natural frequencies in heave and pitch, and both within the typical frequency range of ocean waves (between 4 s and 18 s): when the wave frequency matches either one of the natural frequencies, a large displacement is obtained in the respective DoF, hence nonlinear hydrodynamic coupling; in

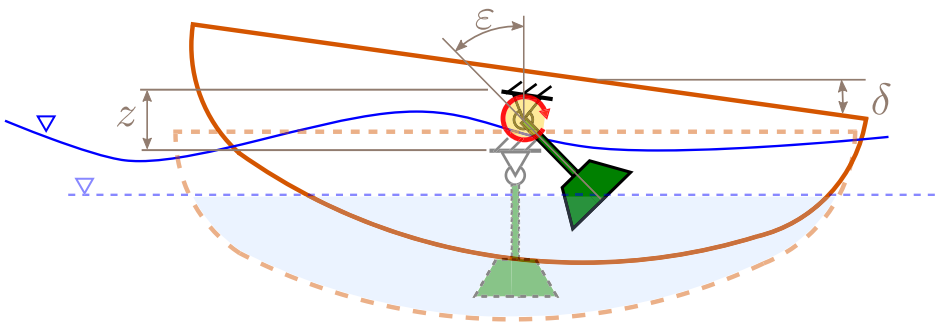

Fig. 2. The floater (in orange) is a waterproof body containing a pendulum (in green), connected to a rotational power take-off (PTO) system (rotating arrow at the hinge). The solid lines show a displaced position in head waves (blue line, with triangle representing the water–air interface), whereas the transparent system with dashed lines shows the resting equilibrium position in still water. The three degrees of freedom have been notionally presented, namely heaving of the centre of mass of the hull (z), pitching of the hull (δ), and rotation of the pendulum and power take-off shaft (ε).

these conditions, thanks to the 2:1 embedded ratio between natural frequencies, there are also the triggering conditions for parametric instability, which increases exponentially until dissipation mechanisms allow.

The use of coupled multiple degrees of freedom is an established way to increase the harvesting performance, at the design stage [69]. Once a design is provided, energy-maximization control strategies attempt to optimally tune the PTO action to maximize performance. Some of such strategies aim at artificially replicating a parametric resonance response [70], such as latching control [71] or time-varying PTO damping coefficients in parametric oscillators [29]. The novelty of the present paper is to embed parametric resonance directly at the design stage; however, it is expected that energy-maximization control strategies retain the potential to further increase the final efficiency, if they are properly informed of the underlying nonlinear phenomenon leading to parametric instability, i.e. if they are based on representative nonlinear models [11].

2.3. Mathematical model

The shape, dimensions, and inertial properties of the system are inspired by [72], as discussed in [61], where the resulting hydrodynamic curves are also reported. The mathematical model is also presented in great detail in [61]; however, a brief and compact description is provided also here, to enable the understanding and interpretation of results.

The objective of this study is to examine the impact of parametric resonance resulting from the nonlinear interaction between the heave and pitch degrees of freedom. To facilitate precise and unambiguous observations, the study employs a carefully selected mathematical model and simulation setup, with specific attention given to eliminating confounding factors and ensuring a clear, transparent, and definitive determination of causality. In particular, the focus of the paper is to study the nonlinear effect of parametric resonance alone; therefore, only the prime nonlinearity responsible of causing parametric instability is included, namely nonlinear Froude–Krylov forces, while all other potential nonlinear effects are disregarded (i.e. viscosity). Similarly, since NLFK and parametric resonance cause a nonlinear coupling between otherwise uncoupled heave and pitch DoFs, a purely heave-pitch hydrodynamic model is considered. Note that nonlinear viscous damping, when present to a significant extent, may have a great influence on parametric resonance [60]; however, for the hull considered in this paper, the assumption of neglecting viscosity is legit, thanks to its smooth and rounded shape along both the heave and pitch degrees of freedom [73].

The consequent linear equation of motion for the hydrodynamic degrees of freedom of the floater is presented hereafter, in the frequency domain:

$$\left[-\omega^2\left(\mathbf{M}+\mathbf{A}(\omega)\right)+j\omega\mathbf{B}(\omega)+\mathbf{K}_h\right]\boldsymbol{\xi}_2=\mathbf{F}_d+\mathbf{F}_{FK_d}, \tag{2}$$

where $\boldsymbol{\xi}_2$ is the (2×1) state vector, composed of heave (z) and pitch (θ), $\mathbf{M}$ the diagonal inertia matrix, $\mathbf{A}(\omega)$ and $\mathbf{B}(\omega)$ the diagonal frequency-dependent added mass and radiation damping, $\mathbf{K}_h$ the diagonal linear hydrostatic stiffness, $\mathbf{F}_d$ and $\mathbf{F}_{FK_d}$ are the diffraction and linear dynamic FK forces, whose sum gives the total hydrodynamic excitation force $\mathbf{F}_{ex}$.

The NLFK version of (2) alternatively computes $\left(\mathbf{F}_{FK_d}-\mathbf{K}_h\boldsymbol{\xi}_2\right)$ in a nonlinear way, as described in Section 3. Solving the nonlinear equation of motion requires to shift from frequency to time domain; to do so, the radiation force is transformed into a convolution integral, which is eventually approximated with a state space equivalent description for computational convenience [74]. Finally, the hydrodynamic model is augmented to include the mechanical coupling with the floater. The resulting augmented state vector is:

$$\boldsymbol{\xi}_{aug}=\left[z,\theta,\dot{z},\dot{\theta},\boldsymbol{k}_z,\boldsymbol{k}_\theta,\varepsilon,\dot{\varepsilon}\right]^T, \tag{3}$$

where ($\boldsymbol{k}_z$ and $\boldsymbol{k}_\theta$) are the auxiliary states to approximate the convolution integral, while ε represents the angular displacement of the pendulum. The full time domain model for the non-autonomous complete system is presented in Appendix A.

The dynamic equation is solved in time domain to evaluate the response of the system, using a second order Runge–Kutta scheme, which has been demonstrated to be appropriate for floating objects and wave energy converters [75]. When the PTO force is included in the dynamic equation, the extracted power is computed as the multiplication of the PTO force and the shaft rotational speed ($\dot{\varepsilon}$).

3. Nonlinear Froude–Krylov force formulation

The phenomenon of parametric resonance arises due to the time-dependent nature of a system's parameters. Considering hydrodynamic interactions, particularly fluid–structure, nonlinear Froude–Krylov (NLFK) forces are therefore a useful numerical tool. These forces are calculated by integrating the pressure of the unperturbed wave field over the instantaneous wetted surface ($S_w(t)$), as follows:

$$\mathbf{f}_{FK}(t)=\mathbf{f}_g+\iint_{S_w(t)}p_u(x,y,z,t)\;\mathbf{n}\;dS, \tag{4a}$$

$$\boldsymbol{\tau}_{FK}(t)=(\mathbf{r}_g-\mathbf{r}_R)\times\mathbf{f}_g+\iint_{S_w(t)}p_u(x,y,z,t)\;(\mathbf{r}-\mathbf{r}_R)\times\mathbf{n}\;dS, \tag{4b}$$

where $\mathbf{f}_g$ is the gravity force, $\boldsymbol{\tau}_g$ its contribution to the torque, $\mathbf{n}$ is the unity vector normal to the surface, $\mathbf{r}$ is the generic position vector, $\mathbf{r}_R=(x_R,y_R,z_R)'$ is the reference point around which the torque is computed, and likewise $\mathbf{r}_g$ is the position vector of the centre of gravity.

For engineering studies that require real-time simulation and multiple iterations in a short time, models with a reasonable computational cost are essential. Axisymmetric and prismatic floaters can benefit from a computationally efficient analytical description of NLFK integrals [76], while geometries with higher complexity may necessitate

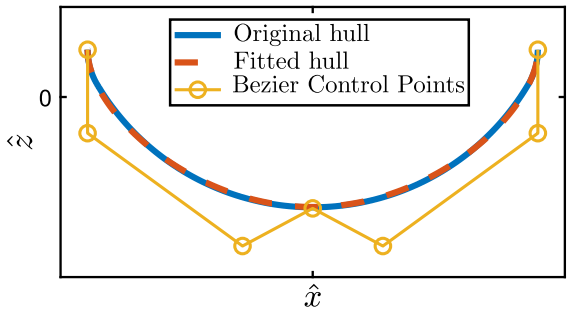

Fig. 3. Cross section in the body-fixed vertical symmetry plane $(\hat{x}, \hat{z})$ of the original hull from [62] and fitted hull via a 6th order symmetric Bezier curve, defined by 7 control points.

the use of mesh-based NLFK methods, which can be computationally intensive. The advantage of axisymmetric and prismatic shapes are to enable an analytical description of the wetted surface $S_w(t)$, hence a close description of the integrals, which are then computed numerically. Moreover, the pressure field is mapped onto a body-fix frame, in order to further simplify the analytical description of the geometry. Body-fix coordinates are marked with a hat: $\hat{\mathbf{r}} = (\hat{x}, \hat{y}, \hat{z})$.

The device being considered in this context is prismatic, meaning that its shape remains invariant in the horizontal direction perpendicular to the wave propagation and parallel to the wave front. Therefore, in a body-fixed frame, a generic point $\hat{\mathbf{r}}$ belonging to the external surface of a prismatic body can be mapped by a change of coordinates $\mathbb{R}^3 \mapsto \mathbb{R}^2$ as: $\hat{\mathbf{r}} = \left(\gamma_x(\alpha), \hat{y}, \gamma_z(\alpha)\right)^\intercal$, with $\alpha \in [\alpha_1, \alpha_2]$ and $\hat{y} \in [\hat{y}_1, \hat{y}_2]$, where the superscript $^\intercal$ stands for the transposition operator, γ_x and γ_z are generic parametric curves, and α is a sweep parameter. Typically, but not necessarily, α goes from 0 to 1 as the directional curve moves from one to the other end. In this paper, such a parametric formulation is used to enable a compact description of the wetted surface by means of a single Bezier curve ($\mathbf{B}$):

$$\mathbf{B}(\alpha) = \sum_{i=0}^{n} \binom{n}{i} (1-\alpha)^{n-i} \alpha^i \mathbf{P}_i, \tag{5}$$

where $\mathbf{P}$ are the defining points of the Bezier curve. The shape of the floater considered in this paper is based on an existing device [62], composed of three tangent circumferences, symmetric about the vertical axis passing through the centre of mass. In this paper, it is proposed to identify the best symmetric Bezier curve, to divide by three the computational effort (see Fig. 3).

According the explicit dependence on α for brevity, the directional vectors are: $\hat{\mathbf{e}}_\alpha = \frac{\partial \hat{\mathbf{r}}}{\partial \alpha} = \left(\gamma_x', 0, \gamma_z'\right)^\intercal$ and $\hat{\mathbf{e}}_{\hat{y}} = \frac{\partial \hat{\mathbf{r}}}{\partial \hat{y}} = (0,1,0)^\intercal$, where the apostrophe indicates the partial derivative with respect to α; thanks to the Bezier curve parametrization, such derivates are polynomials easily derived from (5). The resulting compact description of the Jacobian (J), the normal unity vector ($\hat{\mathbf{n}}$), and the $\left((\hat{\mathbf{r}} - \hat{\mathbf{r}}_R) \times \hat{\mathbf{n}}\right)$ product, as well as the body-fixed forces and torques, are provided in Appendix B.

The correctness of the implementation of the NLFK model has been verified in [76], as well as in the open-access toolbox [77], by means of direct comparison with a benchmark numerical model under controlled simulation conditions (e.g., a displaced floater simulated with a boundary element method solver). In general, the appropriateness of using a NLFK model is legit when the dimensions of the floater are smaller than the characteristics wave lengths [78], hence when the diffraction forces are small compared to the dynamic Froude–Krylov forces [79]; such hypotheses apply to the device herein considered, as shown in [61]. The validation of the NLFK model used in this paper has been performed by comparison with higher fidelity models, such as computational fluid dynamics [80], as well as in experimental campaigns in wave flumes [81]; other, notionally analogous, NLFK models have also been validated, for example for traditional ship hulls using [82], and for wave energy converters [83].

4. Results

This section aims at providing quantitative evidences and understanding of the parametric resonance response of the proposed system, whether it has the potential to bring benefits to the energy conversion performance. To do so, the results should articulate:

- The onset of parametric instability: the conditions that trigger a meaningful parametric resonance response. In the specific mechanical system subject of this paper, these conditions relate to the frequency content of the exciting force and the damping effect of the energy extraction stage performed by the PTO.
- The magnitude of the parametric resonance response: magnitude of the oscillation, especially of the shaft of the PTO, and the consequent useful extracted power.

To achieve these objectives, the results are organized as follows: Section 4.1 presents the response of the system excited at a single frequency (monochromatic wave), either constant in time (harmonic wave) or constantly varying with time (chirp wave). More realistic panchromatic waves are discussed in Section 4.2, considering the effect of the stochastic nature of real ocean waves. In both sections, the free response is first analysed (no PTO), to provide a baseline of the undamped motion, i.e. the highest achievable displacements and nonlinear coupling between different degrees of freedom; then, the effect of various PTO damping parameters is studied.

4.1. Monochromatic waves

In the wave energy field, it is common to initially analyse system responses using regular waves, i.e. monochromatic harmonic functions. This approach may appear intuitive when studying parametric resonance, given its frequency-dependent nonlinearity. Regular waves gradually bring the system to a steady state from equilibrium initial conditions at rest, employing a smoothed excitation force. While regular waves offer physical plausibility, reflecting real waves as a combination of harmonic functions, their monochromatic nature limits exploration of potential bifurcation and hysteresis behaviours. Additionally, comprehensively analysing the wave period (T_w) space can be computationally intensive, necessitating exploration of refined period spacing and lengthy simulations to achieve steady state. Thus, it is advantageous to also consider a physically unrealistic yet informative chirp signal, offering valuable insights into the system's nonlinear behaviour in a computationally efficient manner.

In this paper, a fictitious chirp free surface elevation (η) is considered, with frequency linearly changing with time, defined as:

$$\begin{cases} \eta = \frac{H_w}{2} \cos\left(\left(\frac{c}{2} t + \omega_0\right) t\right) \\ c = \frac{\omega_1 - \omega_0}{T} \end{cases}, \tag{6}$$

where H_w is the wave height and the frequency sweep goes from ω_0 to ω_1 within a time window T, and the consequent instantaneous frequency is $\omega = ct + \omega_0$. Both up-chirp and down-chirp are considered; the range of frequencies goes from 0.8 ω_5 to 2.3 ω_5, where ω_5 is the natural frequency in the pitch DoF. A long T is chosen to guarantee a smooth and slow sweeping of the instantaneous frequency.

It is crucial to emphasize that the chirp signal is imposed on the free surface elevation. Consequently, the wave–structure interaction induces frequency-dependent amplitude modulation and phase shift for the excitation force in the two hydrodynamic degrees of freedom. In the simplified scenario of linear hydrodynamics, the excitation force is formulated using wave-to-force transfer functions, calculated through potential flow solvers, contingent on the wave frequency. In the more realistic scenario of the NLFK model, there is an implicit reliance on the wave height and the displacement of the floater concerning the free surface elevation.

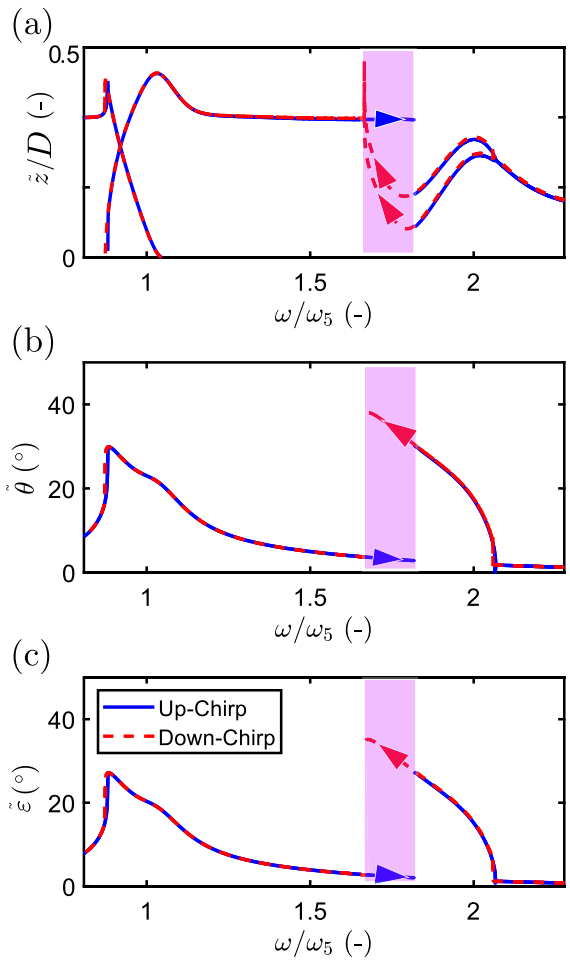

Fig. 4. Free response (no power take-off damping) to up- and down-chirp wave free surface elevations whose frequency (ω) varies linearly with time from 0.8 to 2.3 the pitching natural frequency (ω_5): in (a) the amplitude in heave ($\tilde{z}$) normalized by the draft (D); in (b) the amplitude in pitch ($\tilde{\theta}$); in (c) the amplitude in the pendulum rotation ($\tilde{\varepsilon}$). An hysteresis phenomenon is observed in the response amplitude: the presence of coexisting attractors arising from up- and down-chirp input signals is highlighted by the shaded areas. Arrows notionally indicates the direction of change of the frequency content (rightward in the up-chirp, leftward in the down-chirp).

The outcomes of the up- and down-chirp simulations are illustrated in Fig. 4. The heaving displacement is scaled by the floater's draft (D), while the time traces are depicted against the instantaneous frequency, normalized by the pitching natural frequency (ω_5), as the frequency content linearly increases (or decreases) over time. Given the period-doubling and nonlinear behaviour, defining the amplitude of response becomes ambiguous. Hence, Fig. 4 displays the amplitude ($\tilde{z}$, $\tilde{\theta}$, or $\tilde{\varepsilon}$) determined as the magnitude of the excursion between two consecutive extrema, representing the distance between a maximum and the subsequent minimum.

In the vicinity of the pitching natural period ($\omega/\omega_5 = 1$), the pitch (and pendulum oscillation) exhibit a response curve bending towards lower frequencies, with no discernible hysteresis observed as the responses from up- and down-chirps coincide. Conversely, the heaving response displays a markedly different trend, clearly demonstrating bifurcation near the pitching natural period ($\omega/\omega_5 = 1$) due to period doubling. Hysteresis phenomena become evident closer to the 2:1 parametric resonance region, as evidenced by the presence of two distinct lines in all degrees of freedom. While a smooth transition in amplitude is noted at higher frequencies, an abrupt jump occurs at the lower frequency boundary due to a fold-type bifurcation, wherein an unstable branch exists between two coexisting stable branches. Specifically, while the initiation point of the upper branch remains at the same higher frequency for both sweeping directions, the abrupt jump in the down-chirp response occurs at a considerably lower frequency than in the up-chirp, enlarging the overall instability region.

Results of the free response confirm the presence of the double peak of energy availability, thanks to parametric resonance, as opposed to the single peak that would be foreseen by a linear model. However, energy availability should translate into energy conversion by means of the damping action of a PTO system; such damping may, in principle, hinder the development of parametric instability, hence the generation of the second peak. This is investigated in Fig. 5, where a constant PTO damping parameter (B_{PTO}) is introduced, for different wave periods. Simulations are performed in time domain, considering monochromatic harmonic waves. In order to highlight the enabling effect of nonlinear hydrodynamics (NLFK model), a fully-linear model (LFK) is also shown for comparison. The colour bar represents the steady-state amplitude, defined as the semi-distance trough to peak, of the oscillation of the PTO shaft ($\tilde{\varepsilon}$) and mean extracted power (P); the average is performed at steady state, namely within a time window spanning two wave periods at the end of the time series, in order to encompass the period doubling related to the nonlinear response. The instantaneous extracted power is computed as the product of the PTO force ($B_{PTO}\dot{\varepsilon}$) and the PTO velocity ($\dot{\varepsilon}$).

The LFK model shows a meaningful response, hence power extraction, only around the pitch natural period, which is the unique external excitation mechanism. As the PTO damping increases, the amplitude of motion decreases, while the power extraction first increases and then decreases. Note that a portion of the colour plot is excluded, around $T_w = T_5$, since the amplitude of the pitching angle of the hull becomes too large (more than 50°); this is both unacceptable (capsizing of the hull) and unrealistic, since the linear model is representative only for small displacements of the hydrodynamic DoFs.

Conversely, the NLFK model considers the actual instantaneous wetted surface, hence returns more realistic results. As expected [84], the LFK response is significantly higher than the NLFK response: this is mainly due to the inappropriate underlying hypotheses of the LFK model close to resonance; however, it is worth mentioning that parametric resonance also activates a mechanism for energy leakage from pitch to heave, which decreases, to a minor extent, the energy availability at the PTO axis at the primary linear resonance. The two regions of response are evident in both the angular displacement and power extraction, with comparable values, confirming the relevance for engineering exploitation of the parametric resonance phenomenon; nevertheless, the width of one of the two regions is significantly larger than the other, hence more relevant for energy absorption. As the B_{PTO} increases, the amplitude of motion decreases, as well as the width of the instability region. However, such regions have a pronounced asymmetry, with a sharp outer boundary at higher periods and a smoother edge at lower periods. This is consistent with the trend found in Fig. 4, where the resonance close to $\omega = \omega_5$ has a sharp edge at the lowest frequency (largest period). Finally, it is interesting to highlight that the increase in power extraction is fast as B_{PTO} increases from zero, reaches a maximum, but then remains almost insensitive to further increases of B_{PTO}.

To better visualize the sensitivity to the damping effect of the PTO, Fig. 6 presents isolevel curves for the mean extracted power. The graph clearly shows that the extracted power is zero when B_{PTO} is zero; then, its increase is fast until B_{PTO} is about $3 \cdot 10^6$ Ns/m, while the sensitivity saturates for larger values of B_{PTO}. Conversely, the width of the region of useful power extraction remains relatively constant as B_{PTO} increases. The low sensitivity beyond the maximum power extraction point provides relevant freedom for other engineering objectives, such as the compliance with physical constraints on the displacement of portions of the mechanical system.

Curves provided in Fig. 6 can be used to quantify the relative importance of the 2:1 parametric resonance region, compared to the

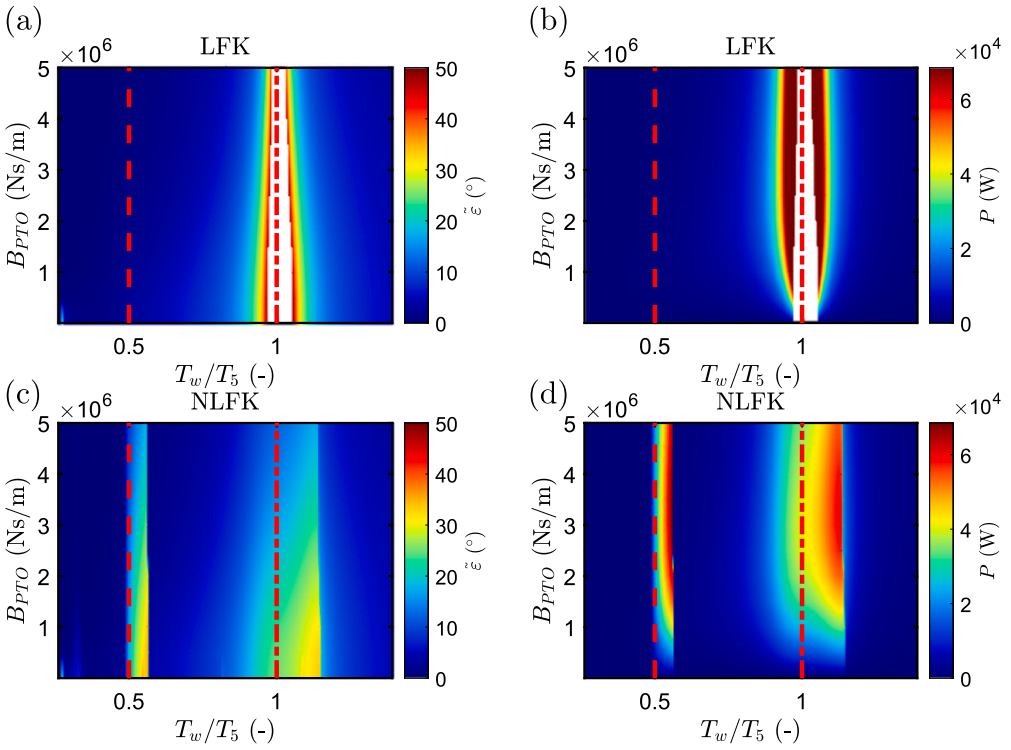

Fig. 5. Amplitude of oscillation of the power take-off shaft ($\tilde{\varepsilon}$, left: panels (a) and (c)) and mean power extracted (P, right: panels (b) and (d)) at steady state with harmonic waves, varying the power take-off damping coefficient (B_{PTO}). Top and bottom rows refer to linear (LFK) and nonlinear (NLFK) Froude–Krylov models, respectively. The dashed and dash-dotted lines highlight T_w/T_5 (ratio between wave excitation period and pitching natural period) equal to 0.5 and 1, respectively. The excluded areas in white around $T_w = T_5$ are due to unrealistic pitching angle ($\tilde{\delta}$), i.e. greater than 50°, where the hydrodynamic linear assumption is not reliable.

natural 1:1 resonance region: although parametric resonance is active in both regions, it is the key enabling factor for the existence of the 2:1 region; therefore, the relative contribution to power production of this second region is a representative indicator of the significance and effectiveness of the parametric resonance embedded by design in the device concept herein studied. Such contributions are computed, for each B_{PTO}, as the integrals of the power curve in Fig. 6, for the 2:1 region when $T_w/T_5 \leq 0.6$, whereas for the 1:1 region when $T_w/T_5 > 0.6$; both values are normalized with the integral of the whole curve. The highest contribution of the 2:1 region is 35.3%, happening when B_{PTO} is the smallest. A more representative value is highlighted by a marker at the optimal B_{PTO} value, namely when the total integral is maximized across the whole range of wave periods: here, the contribution of the 2:1 region is of 25.9%, whereas the 1:1 region covers the remaining 74.1%. Overall, in Fig. 6 the contribution to power extraction of the 2:1 region is always above 25%, corroborating the notion that parametric resonance is indeed effective in increasing the performance of the wave energy converter.

Nevertheless, the sharp edge of the two regions of power extraction, shown in Fig. 6, namely the high sensitivity to the wave period, confirms the anticipated importance of the frequency content of the wave. For this reason, Section 4.2 proceeds with the analysis of more realistic panchromatic waves.

4.2. Panchromatic waves

Real ocean waves are realizations of a stochastic process; in addition, ocean waves are typically described as the superposition of multiple harmonic functions [85]. The literature suggests that it is challenging to achieve high performance of vibration energy harvesters with random [86] or stochastic [87] excitation. In the specific case of wave excitation herein considered, notionally comparing the idealized monochromatic case from Section 4.1 to the more realistic panchromatic case in this section, it is possible to qualitatively anticipate two contrasting effects:

(i) *Positive effect: wider and smoother parametric response regions*. Since every panchromatic wave excitation is composed of multiple frequency components, the sharp edges observed in Figs. 4 to 6 are likely disappearing, hence decreasing the critically high sensitivity to the wave period.

(ii) *Negative effect: lower amplitude and extracted power*. Considering a frequency within the instability region, the monochromatic wave is likely the most effective in causing a parametric resonance response because, at every wave cycle, it consistently pumps energy into the system and gradually drives it into instability. Conversely, a panchromatic wave has its spectral energy distributed across various frequency components, some of which are different from the nominal parametric resonance frequency; in addition, considering the variability across consecutive wave cycles of the specific time trace of the stochastic realization, there may be portions of the signals that favour the parametric resonance response, while other portions that prematurely break the build-up of instability instead.

The objective of this section is to provide a quantitative analysis of such qualitative effects in order to assess if the proposed mechanical system remains relevant for engineering applications also with realistic panchromatic waves, i.e. if the decrease in power extraction is acceptable or drastic. To do so, a JONSWAP (Joint North Sea Wave Observation Project) wave spectrum is considered [88], normally used for not fully-developed sea.

Based on the findings from the monochromatic simulations illustrated in Fig. 5, the focus is directed towards the region surrounding the 2:1 parametric resonance configuration. Note that the design for realizing a device prone to 2:1 parametric resonance is unchanged, since it is independent of exogenous factors such as the type of wave excitation, but it depends only on the mass, inertia and stiffness of the system, such that the natural period in pitch is twice that in heave.

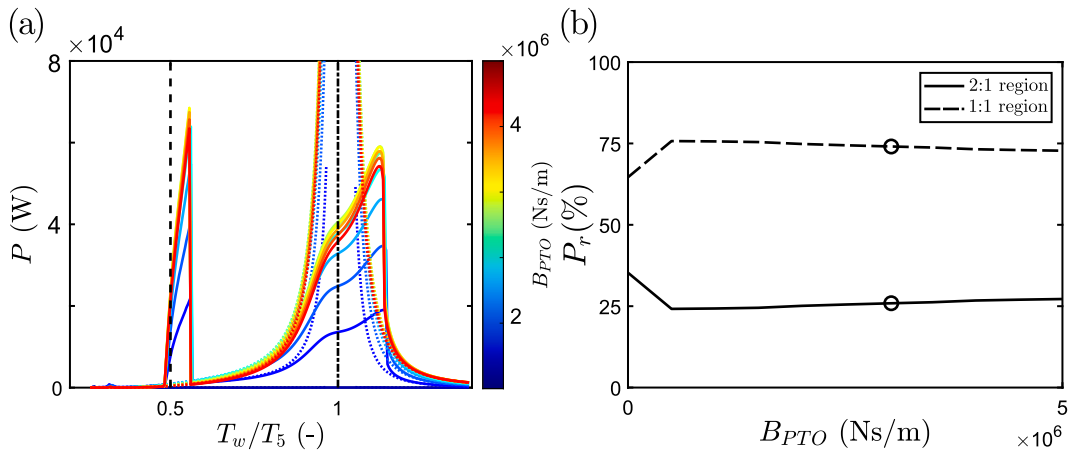

Fig. 6. Panel (a) on the left: sensitivity of the mean extracted power (P) to the power take-off damping coefficient (B_{PTO}) with harmonic waves, according to linear (dotted lines) and nonlinear (solid lines) models; the dashed and dash-dotted lines highlight T_w/T_5 (ratio between wave excitation period and pitching natural period) equal to 0.5 and 1, respectively. Panel (b) on the right: P_r is the ratio of the area below the mean extracted power curve, in the 2:1 region (for $T_w/T_5 \leq 0.6$) with the solid line, in the 1:1 region (for $T_w/T_5 > 0.6$) with dashed line; the circle marker stands for the best B_{PTO}, i.e. that maximizes the area below the full frequency range of the curve, indicating maximum energy extraction.

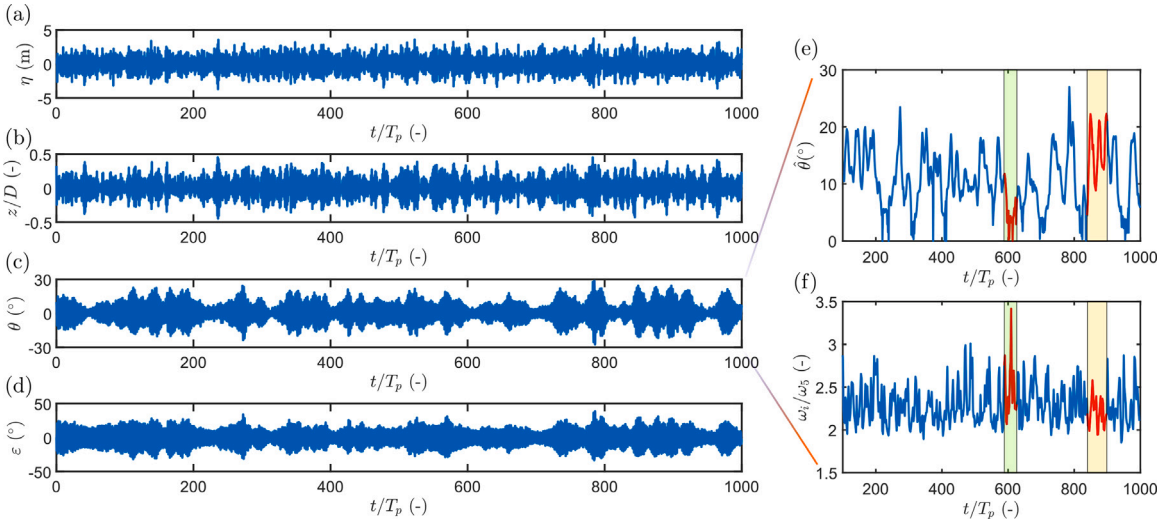

Fig. 7. On the left, panels from (a) to (d): time series of the free (no power take-off damping) dynamic response to a panchromatic wave under parametric resonance conditions, with a peak period (T_p) equal to 0.52 times the natural period in pitch (T_5) and a significant wave height (H_s) equal to 0.66 times the draft (D); panel (a) shows the free surface elevation (η), panel (b) the normalized heaving displacement (z/D), panel (c) the hull pitching angle (θ), and panel (d) the pendulum oscillation angle (ε). On the right: panel (e) shows the consecutive amplitudes of the pitching angle ($\hat{\theta}$), defined as the semi-distance between two consecutive peaks (maxima) and troughs (minima); panel (f) shows the instantaneous frequency (ω_i), defined in (7), normalized by the pitching natural frequency (ω_5); the shaded areas in (e) and (f) highlight examples of regions where the pitching response is either small (green) or large (yellow).

Consequently, the peak period (T_p) is set to 0.52 T_5, while the significant wave height (H_s) is 0.66 D. Panchromatic waves are generated using a deterministic amplitude and random phase approach [85]; in fact, due to its stochastic nature, the results exhibit variability across different realizations. This variability is typically addressed by employing either multiple short realizations or a single long one. In this study, the latter approach is first adopted to produce results that reflect a complete sea state in real-world conditions. Specifically, 1000 peak periods are simulated, with a brief initial ramp of 5 peak periods. Over the extended duration of this simulation, the aim is to explore the occurrence and location of parametric resonance.

Fig. 7 depicts the resultant time series of the free response. It is noteworthy that the time axis is normalized by the peak period, and the vertical displacement is normalized by the floater's draft. The variability observed in the heave response closely mirrors that of the free surface, as anticipated. Of particular interest is the substantial nonlinear parametric resonance response, evident in both pitch and consequently in the PTO rotation, across significant portions of the time series. Thus, it is interesting to remark that the build-up of instability does not seem to be hindered by the presence of multiple frequencies. However, there are discernible areas with relatively minor parametric responses, while others exhibit sustained pitch angles. For instance, in region around 600 T_p, the pitch response is minimal and diminishing: insufficient parametric resonance hinders the transfer of energy from heave to pitch, resulting in the gradual dissipation of accumulated energy in the pitch degree of freedom. Conversely, for example in the region just before 900 T_p, the brief decaying segments are promptly interrupted by subsequent instability builds-up, leading to a sustained high pitching motion over an extended time span.

It is essential to ascertain the underlying causes of these discrepancies to comprehend the reliability of parametric resonance as an energy conversion mechanism. Evidently, the 2:1 frequency condition, applicable in the case of regular waves, does not suffice to fully elucidate the parametric resonance response in irregular conditions. Therefore, to gain deeper insights into the likelihood of parametric resonance occurrence, a quantitative metric is herein proposed. Considering that

frequency remains the primary driver of instability, it is intuitive to explore a more localized frequency descriptor that may exhibit correlation with the magnitude of parametric response. Hence, the *instantaneous frequency* (ω_i) of the incoming wave is examined, defined as the first conditional spectral moment of the time–frequency distribution [89], computed as follows:

$$\omega_i = 2\pi \frac{\int_0^\infty f\, S(t,f) df}{\int_0^\infty S(t,f) df}, \tag{7}$$

where f represents the frequency in Hertz, and $S(t,f)$ denotes the spectrogram power spectrum as a time–frequency distribution [90]. To compute the time-dependent spectrum, the signal undergoes division into overlapping segments, with each segment subjected to filtering windows to prevent leakages. Subsequently, a short-time Fourier transform is applied to each segment. Fig. 7 illustrates the resulting instantaneous frequency, plotted against consecutive amplitudes of the pitching angle ($\hat{\theta}$), defined as the semi-distance between two consecutive peaks (maxima) and troughs (minima). The shaded areas represent examples of regions where the pitching response (bottom figure) due to parametric resonance is either small (green area, close to 600 T_p) or large (yellow area, close to 900 T_p). It is evident that regions of substantial and sustained parametric response align with a normalized instantaneous frequency (top figure) relatively close to the ratio of 2. Conversely, when the instantaneous frequency deviates from this ratio, the pitching response rapidly diminishes. This observation corroborates the conceptual understanding derived from the simplified scenario of monochromatic waves. However, Fig. 7 also implies that the variability of ω_i along the time evolution of the excitation signal is an additional crucial parameter to evaluate the likelihood of the build-up of a sustained response for useful power extraction.

Since panchromatic waves are generated from a stochastic process, multiple realizations should be analysed for each wave condition, in order to be exposed to enough variability; to do so, common options usually are to either consider a few long time series, or many shorter signals [85]. While such approaches are often equivalent in terms accuracy of the predicted results, their computational time may differ. Due to the Nyquist sampling theorem, the longer in time the signal is, the smallest the sampling frequency, hence the higher the number of frequency components. Although this is usually irrelevant in linear simulations, the NLFK model computes the undisturbed pressure field and the free surface elevation at every time step as the superposition of the full range of frequency components; moreover, such calculation is iterated within the recursive numerical integration algorithm until certain relative and absolute tolerances are met. Thus, the computational time of the NLFK is highly sensitive to the number of frequency components.

Fig. 8 shows an example of the resulting relative computational time, defined as the ratio between the simulation and simulated time, i.e. a proxy of the real-time computing ability of the NLFK model (≤ 1). The same sea state of the time series of Fig. 7 is considered. While the long simulation lasts for 1000 T_p, short simulations are 10-fold shorter (i.e., 100 T_p). The number of realizations for the short time series are set to 10 to reduce uncertainties, while only 4 realizations of the long simulation are considered, due to the high computational time. The resulting mean relative computational time is one order of magnitude higher for the long simulation, specifically 5.7 compared to 0.59.

On the one hand, short simulations are clearly advantageous from the computational time perspective; on the other hand, it should be assessed whether the long time series are necessary to appreciate enough variability. The plot in Fig. 7 already provides a visual evidence of the relatively fast dynamics of parametric resonance, which builds-up and breaks-down in time windows much shorter than the whole simulation time; moreover, there are several instances of time series portions where both high and low pitching response appear. To further corroborate this, results obtained with four different long realizations are compared in Fig. 9, considering the probability of occurrence ($\mathcal{P}$)

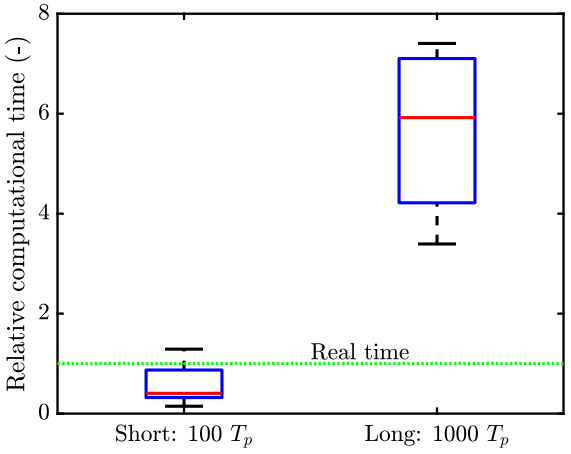

Fig. 8. Box plot of the relative computational time, defined as the ratio between simulation time and run time, computed for 10 short realizations and 4 long realizations of the panchromatic wave presented in Fig. 7, where T_p is the wave peak period. The green dotted line represents the threshold for real time computation, i.e. when the relative computational time is unity.

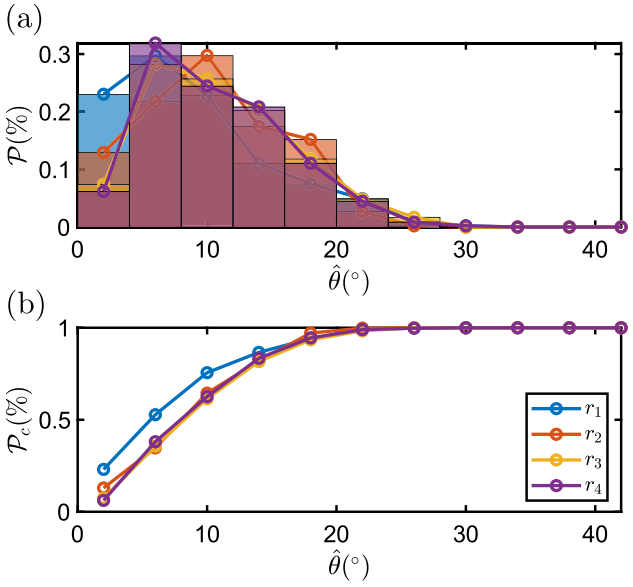

Fig. 9. Probability ($\mathcal{P}$, panel (a)) and cumulative probability ($\mathcal{P}_c$, panel (b)) of the peak-to-trough amplitude of the free response pitching angle ($\hat{\theta}$) for 4 long (1000 T_p) realizations (r_i) of the same sea state as in Fig. 7, where T_p is the wave peak period. The width of the bins is 4°.

of the pitching angle amplitudes, induced by parametric resonance; the width of the bins is 4°. It is especially clear from the cumulative probability ($\mathcal{P}_c$), complementary to the probability of exceedance, that all realizations have similar statistics, with small exception for the first realization (r_1). Therefore, it can be inferred that the build-up of parametric instability is likely to appear for most of conditions in real wave scenarios; in fact, sea states are typically stationary and ergodic within 1000 wave periods, which range between 1 and 3 h.

For simulation purposes, however, it would be advantageous to consider shorter simulations, as shown in Fig. 8, as long as the predicted results are representative of the actual response to realistic long sea states. This is investigated in Fig. 10, where 10 short simulations (100 T_p) are run for every wave period, at constant wave height and PTO damping coefficient. Being an irregular sea condition, the vertical axis represent the standard deviation (σ) of the 3 DoFs; the solid line presents the mean across the 10 realizations, which are

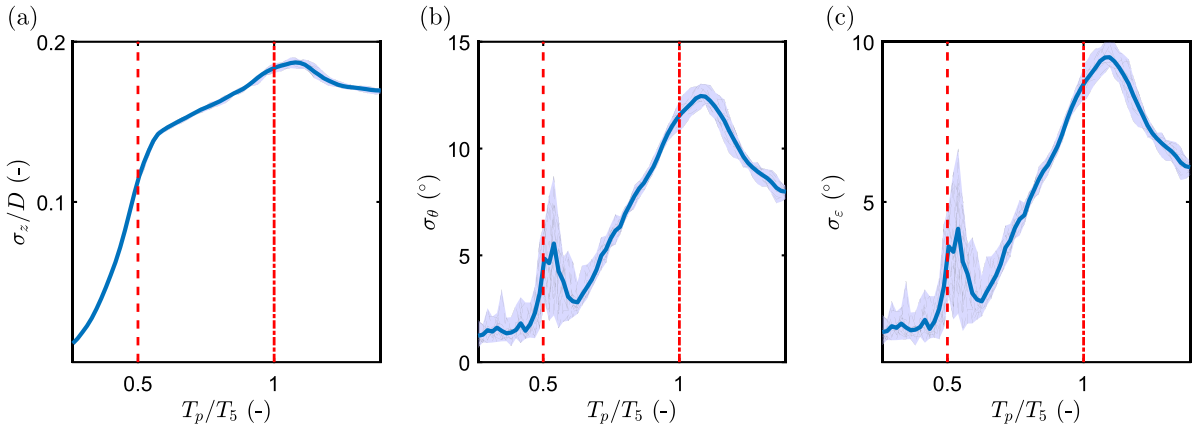

Fig. 10. Standard deviation (σ, solid line) and envelope (shaded area) of responses (thin dashed grey lines) to 10 realizations of short (100 T_p) irregular waves, with constant $H_s = 0.66\ D$ and B_{PTO} of $3 \cdot 10^6$ Ns/m, in heave (panel (a)), pitch (panel (b)), and power take-off rotation (panel (c)). The dashed and dash-dotted lines highlight T_p/T_5 equal to 0.5 and 1, respectively.

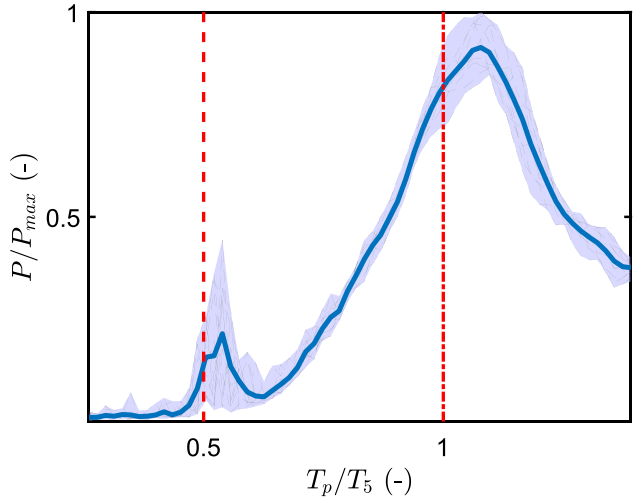

Fig. 11. Mean normalized converted power (solid line) and envelope (shaded area), computed for 10 realizations (thin dashed grey lines) of short (100 T_p) irregular waves, with constant significant wave height ($H_s = 0.66\ D$) and power take-off coefficient (B_{PTO}) of $3 \cdot 10^6$ Ns/m. The dashed and dash-dotted lines highlight T_p/T_5 equal to 0.5 and 1, respectively.

individually plotted in dashed light-grey lines and encompassed in a shaded envelope, to convey the information of variability.

The standard deviation of the heaving response (σ_z) is remarkably constant across all 10 realizations, as the envelope is barely distinguishable only close to the pitching natural period. Conversely, a high variability is seen in the pitching (σ_θ) and PTO rotation (σ_ε) standard deviations, particularly in the 2:1 parametric instability region. Despite the variability, the average trend confirms the existence of the two peaks, hence corroborating the suitability of multiple short simulations for numerical analysis. The numerical model is then used to evaluate the variability of the power production, shown in Fig. 11 in normalized form.

Consistently with Fig. 10, higher variability is found close to the two parametric resonance frequencies. The second region of power extraction, enabled by the 2:1 design herein proposed, is found to be smaller but significant, since it is comparable to the internal resonance region; however, the ratio between the two highest peaks is about 40%, while the ratio between the maxima of the average trends is about 25%. Although positive, it is worth comparing such results with those predicted under regular wave conditions, shown in Fig. 6, where the maximum magnitude of power extraction was about the same in both regions of parametric resonance. The significant drop in relative performance between the two regions under irregular wave conditions is mostly due to the narrow width of the 2:1 region, which makes power conversion effective only when the instantaneous frequency (ω_i), shown in Fig. 7, is very close to the parametric resonance ratio.

5. Conclusion

This paper investigates the modelling and performance of a mechanical system for wave energy conversion based on hydrodynamic parametric resonance. A 2:1 instability is embedded in the inertial properties, such that a second region of power extraction is enabled, in addition to the natural resonance region. More specifically, this paper focuses on some modelling aspects of hydrodynamic parametric resonance, especially considering the effect of including actual power extraction and realistic panchromatic waves.

Starting from the baseline of the free response to monochromatic waves, it is shown that parametric resonance indeed generates a second region of available mechanical power. Moreover, the inclusion of Power Take-Off (PTO) damping for power extraction does not prevent the development of parametric resonance; in addition, the peak power conversion in the two regions is similar, although the 2:1 region is much narrower and with sharp boundaries.

Beneficial parametric resonance is also preserved going from regular to irregular waves. However, apart from the peak period of the panchromatic wave spectrum, it is demonstrated that additional factors must be counted in, namely the instantaneous frequency and the length of the time trace. The severity of parametric resonance is found to be dependent on the time-variability of the instantaneous frequency: when it is about constant and close to the 2:1 ratio, the parametric response is high; conversely, when it is consistently further away from the 2:1 ratio, the parametric response is low.

Although very long simulations are more representative of real sea conditions and show less variability, under the nonlinear Froude–Krylov force framework needed to describe the hydrodynamic parametric resonance, long simulations are one order of magnitude more computationally demanding. Many short simulations, although more variable, return consistent average predictions and are therefore suitable for numerical simulations.

Power extraction remains promising also under irregular wave conditions. However, the energy obtained in the second region created by design at the 2:1 parametric resonance is between 60% and 75% lower

than the power absorption within the natural frequency region. Despite such a reduction, this represents an encouraging baseline to be leveraged by a properly informed energy-maximization control strategy, able to drive the system to enhance the response to the advantageous frequency components while filtering out the others. Future directions for further research encompass the techno–economic modelling and design of a system able to experience 2:1 resonance in a typical wave climate of an offshore location: the next step is to study the interplay between physical constraints, hydrodynamic behaviour depending on the wetted surface, mass and inertial properties, and the related capital and operational expenditures.

CRediT authorship contribution statement

Giuseppe Giorgi: Writing – review & editing, Writing – original draft, Visualization, Validation, Supervision, Software, Resources, Project administration, Methodology, Investigation, Funding acquisition, Formal analysis, Data curation, Conceptualization.

Declaration of competing interest

The authors declare that they have no known competing financial interests or personal relationships that could have appeared to influence the work reported in this paper.

Data availability

Data will be made available on request.

Acknowledgements

Project funded under the National Recovery and Resilience Plan (NRRP), Italy, Mission 4 Component 2 Investment 1.3 - Call for tender No. 1561 of 11.10.2022 of Ministero dell' Universitá e della Ricerca (MUR); funded by the European Union – NextGenerationEU Award Number: Project code PE0000021, Concession Decree No. 1561 of 11.10.2022 adopted by Ministero dell'Universitá e della Ricerca (MUR), Italy, CUP, Italy E13C22001890001, Project title "Network 4 Energy Sustainable Transition – NEST".

Appendix A

The full time domain model for the non-autonomous complete system is described by the following first order differential equation:

$$\hat{\mathbf{M}}\dot{\boldsymbol{\xi}}_{aug} = \hat{\mathbf{A}}\boldsymbol{\xi}_{aug} + \hat{\mathbf{F}}_{ex}, \tag{A.1}$$

where $\hat{\mathbf{F}}_{ex} \in \mathbb{R}^{\hat{N}\times 1}$ is non-zero only in the third and fourth dimensions, where the external hydrodynamic forces act on the heave and pitch DoFs. Likewise, $\hat{\mathbf{M}} \in \mathbb{R}^{\hat{N}\times\hat{N}}$ is defined as follows:

$$\hat{\mathbf{M}} = \begin{bmatrix} \mathbf{1}_{2\times 2} & & & & \\ & M_h + \mathbf{A}^z_\infty & & & \\ & & I_\delta + \mathbf{A}^\theta_\infty - 2mdl & & I_y + ml^2 - mdl \\ & & & \mathbf{1}_{8\times 8} & \\ & & I_y + ml^2 - mdl & & I_y + ml^2 \end{bmatrix}, \tag{A.2}$$

and zero otherwise, where $\mathbf{1}_{n\times n}$ is the squared identity diagonal matrix of dimension n, M_h is the hull mass and I_δ its inertia, m is the pendulum mass and I_y its inertia about its hinge, l is the pendulum length and d its distance from the hull's centre of gravity; $\mathbf{A}^z_\infty$ and $\mathbf{A}^\theta_\infty$ are the added mass at infinite frequency in the heave and pitch DoFs, respectively.

Finally, $\hat{\mathbf{A}}$ is composed as follows:

$$\hat{\mathbf{A}} = \begin{bmatrix} & & 1 & & & & & \\ & & & 1 & & & & \\ -\mathbf{K}^z_h & & & & -\mathbf{C}^{ss}_z & & & \\ & -\mathbf{K}^\theta_h + mg(d-l) & & & & -\mathbf{C}^{ss}_\theta & -mgl & \\ & & \mathbf{B}^{ss}_z & & \mathbf{A}^{ss}_z & & & \\ & & & \mathbf{B}^{ss}_\theta & & \mathbf{A}^{ss}_\theta & & 1 \\ & -mgl & & & & & -mgl & -B_p \end{bmatrix}, \tag{A.3}$$

and zero otherwise, where B_p is a small friction coefficient at the pendulum hinge, and $\mathbf{K}^z_h$ and $\mathbf{K}^\theta_h$ are the added mass at infinite frequency in the heave and pitch DoFs, respectively. Note that, in the NLFK case, $\mathbf{K}_h$ is computed within the nonlinear framework of Section 3, so it is removed from $\hat{\mathbf{M}}$.

Further details about the mathematical model, as well as the quantitative values of all of the system parameters, are provided in [61].

Appendix B

The directional vectors can be used to compute the Jacobian (J), the normal unity vector ($\hat{\mathbf{n}}$), and the $((\hat{\mathbf{r}} - \hat{\mathbf{r}}_R) \times \hat{\mathbf{n}})$ product:

$$J = \|\hat{\mathbf{e}}_{\hat{x}} \times \hat{\mathbf{e}}_{\hat{y}}\| = \sqrt{\gamma_x'^2 + \gamma_z'^2}, \tag{B.1a}$$

$$\hat{\mathbf{n}} = \frac{\hat{\mathbf{e}}_{\hat{x}} \times \hat{\mathbf{e}}_{\hat{y}}}{\|\hat{\mathbf{e}}_{\hat{x}} \times \hat{\mathbf{e}}_{\hat{y}}\|} = \frac{1}{\sqrt{\gamma_x'^2 + \gamma_z'^2}} \begin{pmatrix} -\gamma_z' \\ 0 \\ \gamma_x' \end{pmatrix}, \tag{B.1b}$$

$$(\hat{\mathbf{r}} - \hat{\mathbf{r}}_R) \times \hat{\mathbf{n}} = \frac{1}{\sqrt{\gamma_x'^2 + \gamma_z'^2}} \begin{pmatrix} \gamma_x' (\hat{y} - \hat{y}_R) \\ -\gamma_x'(\gamma_x - \hat{x}_R) - \gamma_z'(\gamma_z - \hat{z}_R) \\ \gamma_z' (\hat{y} - \hat{y}_R) \end{pmatrix}. \tag{B.1c}$$

Applying the change of variables of (B.1) to the integral formulation in (4), the resulting body-fixed forces and torques become:

$$\hat{\mathbf{f}}_p(t) = W \int_{\alpha_1}^{\alpha_2} p_u(\gamma_x(\alpha), \gamma_z(\alpha), t) \begin{pmatrix} -\gamma_z' \\ 0 \\ \gamma_x' \end{pmatrix} d\alpha, \tag{B.2a}$$

$$\hat{\boldsymbol{\tau}}_p(t) = W \int_{\alpha_1}^{\alpha_2} p_u(\gamma_x(\alpha), \gamma_z(\alpha), t) \begin{pmatrix} 0 \\ -\gamma_x'(\gamma_x - \hat{x}_R) - \gamma_z'(\gamma_z - \hat{z}_R) \\ 0 \end{pmatrix} d\alpha, \tag{B.2b}$$

where W is the width of the floater in the $\hat{y}$ direction. Then, appropriate rotation matrices are applied to map the undisturbed pressure field and free surface elevation from the world- to the body-frame, as described in [62].

References

[1] Terrero González A, Dunning P, Howard I, McKee K, Wiercigroch M. Is wave energy untapped potential? Int J Mech Sci 2021;205:106544. http://dx.doi.org/10.1016/J.IJMECSCI.2021.106544.

[2] Clemente D, Rosa-Santos P, Taveira-Pinto F. On the potential synergies and applications of wave energy converters: A review. Renew Sustain Energy Rev 2021;135:110162. http://dx.doi.org/10.1016/j.rser.2020.110162.

[3] Commission E. An EU strategy to harness the potential of offshore renewable energy (ORE) for a climate neutral future, EUR-Lex - 52020dc0741 – EN, COM/2020/741. 2020.

[4] Ruiz-Minguela P, Blanco JM, Nava V, Jeffrey H. Technology-agnostic assessment of wave energy system capabilities. Energies 2022;15(7):2624. http://dx.doi.org/10.3390/EN15072624.

[5] Onea F, Rusu E. An evaluation of marine renewable energy resources complementarity in the Portuguese nearshore. J Mar Sci Eng 2022;10(12):1901. http://dx.doi.org/10.3390/JMSE10121901.

[6] Robertson B, Bekker J, Buckham B. Renewable integration for remote communities: Comparative allowable cost analyses for hydro, solar and wave energy. Appl Energy 2020;264:114677. http://dx.doi.org/10.1016/J.APENERGY.2020.114677.

[7] Guo C, Sheng W, De Silva DG, Aggidis G. A review of the levelized cost of wave energy based on a techno–economic model. Energies 2023;16(5):2144. http://dx.doi.org/10.3390/EN16052144.

[8] Giglio E, Petracca E, Paduano B, Moscoloni C, Giorgi G, Sirigu SA. Estimating the cost of wave energy converters at an early design stage: A bottom-up approach. Sustainability 2023;15(8):6756. http://dx.doi.org/10.3390/SU15086756.
[9] Zheng S, Zhang Y, Iglesias G. Concept and performance of a novel wave energy converter: Variable aperture point-absorber (VAPA). Renew Energy 2020;153:681–700. http://dx.doi.org/10.1016/j.renene.2020.01.134.
[10] Olbert G, Abdel-Maksoud M. High-fidelity modelling of lift-based wave energy converters in a numerical wave tank. Appl Energy 2023;347:121460. http://dx.doi.org/10.1016/J.APENERGY.2023.121460.
[11] Faedo N, Giorgi G, Ringwood JV, Mattiazzo G. Optimal control of wave energy systems considering nonlinear Froude–Krylov effects: Control-oriented modelling and moment-based control. Nonlinear Dynam 2022;109(3):1777–804. http://dx.doi.org/10.1007/s11071-022-07530-3.
[12] Zhang L, Draycott S, Stansby P. System identification and generalisation of elastic mooring line forces on a multi-float wave energy converter platform in steep irregular waves. Mech Syst Signal Process 2024;214:111259. http://dx.doi.org/10.1016/j.ymssp.2024.111259.
[13] Al Shami E, Wang Z, Wang X. Non-linear dynamic simulations of two-body wave energy converters via identification of viscous drag coefficients of different shapes of the submerged body based on numerical wave tank CFD simulation. Renew Energy 2021;179:983–97. http://dx.doi.org/10.1016/J.RENENE.2021.07.068.
[14] da Silva LSP, Cazzolato BS, Sergiienko NY, Ding B, Morishita HM, Pesce CP. Statistical linearization of the Morison's equation applied to wave energy converters. J Ocean Eng Mar Energy 2020;1–13. http://dx.doi.org/10.1007/s40722-020-00165-9.
[15] Windt C, Davidson J, Ransley EJ, Greaves D, Jakobsen M, Kramer M, et al. Validation of a CFD-based numerical wave tank model for the power production assessment of the wavestar ocean wave energy converter. Renew Energy 2020;146:2499–516. http://dx.doi.org/10.1016/j.renene.2019.08.059.
[16] Ropero-Giralda P, Crespo AJ, Tagliafierro B, Altomare C, Domínguez JM, Gómez-Gesteira M, et al. Efficiency and survivability analysis of a point-absorber wave energy converter using DualSPHysics. Renew Energy 2020;162:1763–76. http://dx.doi.org/10.1016/j.renene.2020.10.012.
[17] Wei N, Zhang Z, Cheng G, Yang H, Hu Y, Wen J. Study of a vortex-induced vibration piezoelectric wind energy harvester based on the synergy of multi-degree-of-freedom technology and magnetic nonlinear technology. Mech Syst Signal Process 2024;214:111381. http://dx.doi.org/10.1016/J.YMSSP.2024.111381.
[18] Postnikov A, Pavlovskaia E, Wiercigroch M. 2DOF CFD calibrated wake oscillator model to investigate vortex-induced vibrations. Int J Mech Sci 2017;127:176–90. http://dx.doi.org/10.1016/J.IJMECSCI.2016.05.019.
[19] Giorgi G, Davidson J, Habib G, Bracco G, Mattiazzo G, Kalmár-nagy T. Nonlinear dynamic and kinematic model of a spar-buoy : Parametric resonance and yaw numerical instability. J Mar Sci Eng 2020;8(504):1–17. http://dx.doi.org/10.3390/jmse8070504.
[20] Fan T, Qiao D, Yan J, Chen C, Ou J. An improved quasi-static model for mooring-induced damping estimation using in the truncation design of mooring system. Ocean Eng 2017;136:322–9. http://dx.doi.org/10.1016/J.OCEANENG.2016.05.042.
[21] Mukundan H, Modarres-Sadeghi Y, Dahl JM, Hover FS, Triantafyllou MS. Monitoring VIV fatigue damage on marine risers. J Fluids Struct 2009;25(4):617–28. http://dx.doi.org/10.1016/J.JFLUIDSTRUCTS.2009.03.003.
[22] Tarrant KR, Meskell C. Investigation on parametrically excited motions of point absorbers in regular waves. Ocean Eng 2016;111:67–81. http://dx.doi.org/10.1016/j.oceaneng.2015.10.041.
[23] Naseer R, Abdelkefi A. Nonlinear modeling and efficacy of VIV-based energy harvesters: Monostable and bistable designs. Mech Syst Signal Process 2022;169:108775. http://dx.doi.org/10.1016/J.YMSSP.2021.108775.
[24] Wan C, Tian H, Shan X, Xie T. Enhanced performance of airfoil-based piezoelectric energy harvester under coupled flutter and vortex-induced vibration. Int J Mech Sci 2023;241:107979. http://dx.doi.org/10.1016/J.IJMECSCI.2022.107979.
[25] Jia Y. Review of nonlinear vibration energy harvesting: Duffing, bistability, parametric, stochastic and others. J Intell Mater Syst Struct 2020;31(7):921–44. http://dx.doi.org/10.1177/1045389X20905989.
[26] Raj PV, Santhosh B. Parametric study and optimization of linear and nonlinear vibration absorbers combined with piezoelectric energy harvester. Int J Mech Sci 2019;152:268–79. http://dx.doi.org/10.1016/J.IJMECSCI.2018.12.053.
[27] Nie X, Pei S, Tan T, Yan Z, Yan Z. Nonlinear 1:2 internal resonance response of L-shaped piezoelectric energy harvester under the influence of electrical damping. Int J Mech Sci 2022;225:107365. http://dx.doi.org/10.1016/J.IJMECSCI.2022.107365.
[28] Chen M, Xiao P, Zhang Z, Sun L, Li F. Effects of the end-stop mechanism on the nonlinear dynamics and power generation of a point absorber in regular waves. Ocean Eng 2021;242. http://dx.doi.org/10.1016/J.OCEANENG.2021.110123.
[29] Giorgi G, Faedo N. Performance enhancement of a vibration energy harvester via harmonic time-varying damping: A pseudospectral-based approach. Mech Syst Signal Process 2022;165:108331. http://dx.doi.org/10.1016/J.YMSSP.2021.108331.
[30] Liu D, Wu Y, Xu Y, Li J. Stochastic response of bistable vibration energy harvesting system subject to filtered Gaussian white noise. Mech Syst Signal Process 2019;130:201–12. http://dx.doi.org/10.1016/j.ymssp.2019.05.004.
[31] Devarajan K, Santhosh B. Performance enhancement of snap-through vibration energy harvester with displacement amplifier. Int J Mech Sci 2023;253:108391. http://dx.doi.org/10.1016/J.IJMECSCI.2023.108391.
[32] Yang W, Towfighian S. A parametric resonator with low threshold excitation for vibration energy harvesting. J Sound Vib 2019;446:129–43. http://dx.doi.org/10.1016/J.JSV.2019.01.038.
[33] Nolis GM, Yang H, Chernova NA, Zhang R, Omenya F, et al. Internal resonance and low frequency vibration energy harvesting. Smart Mater Struct 2017;26(9):095008. http://dx.doi.org/10.1088/1361-665X/AA791D.
[34] Daqaq MF, Giorgi G, Khasawneh MA, Daqaq MF, Network G, Giorgi G. Deliberate introduction of a nonlinear restoring element to point wave energy absorbers: A review and assessment. Nonlinear Dynam 2024;2024:1–37. http://dx.doi.org/10.1007/S11071-024-09794-3.
[35] Daqaq MF, Masana R, Erturk A, Quinn DD. On the role of nonlinearities in vibratory energy harvesting: A critical review and discussion. Appl Mech Rev 2014;66(4). http://dx.doi.org/10.1115/1.4026278/472587.
[36] Khasawneh MA, Daqaq MF. Experimental assessment of the performance of a bi-stable point wave energy absorber under harmonic incident waves. Ocean Eng 2023;280:114494. http://dx.doi.org/10.1016/J.OCEANENG.2023.114494.
[37] Zhang X, Yang J. Power capture performance of an oscillating-body WEC with nonlinear snap through PTO systems in irregular waves. Appl Ocean Res 2015;52:261–73. http://dx.doi.org/10.1016/J.APOR.2015.06.012.
[38] Zhang X, Tian XL, Xiao L, Li X, Lu W. Mechanism and sensitivity for broadband energy harvesting of an adaptive bistable point absorber wave energy converter. Energy 2019;188:115984. http://dx.doi.org/10.1016/J.ENERGY.2019.115984.
[39] Wu Z, Levi C, Estefen SF. Practical considerations on nonlinear stiffness system for wave energy converter. Appl Ocean Res 2019;92:101935. http://dx.doi.org/10.1016/J.APOR.2019.101935.
[40] Xi R, Zhang H, DaolinXu, Zhao H, Mondal R. High-performance and robust bistable point absorber wave energy converter. Ocean Eng 2021;229:108767. http://dx.doi.org/10.1016/J.OCEANENG.2021.108767.
[41] Younesian D, Alam MR. Multi-stable mechanisms for high-efficiency and broadband ocean wave energy harvesting. Appl Energy 2017;197:292–302. http://dx.doi.org/10.1016/J.APENERGY.2017.04.019.
[42] Zhang H, Xi R, Xu D, Wang K, Shi Q, Zhao H, et al. Efficiency enhancement of a point wave energy converter with a magnetic bistable mechanism. Energy 2019;181:1152–65. http://dx.doi.org/10.1016/J.ENERGY.2019.06.008.
[43] Zhou K, Dai HL, Abdelkefi A, Ni Q. Theoretical modeling and nonlinear analysis of piezoelectric energy harvesters with different stoppers. Int J Mech Sci 2020;166:105233. http://dx.doi.org/10.1016/J.IJMECSCI.2019.105233.
[44] Zhang X, Zhang H, Zhou X, Sun Z. Recent advances in wave energy converters based on nonlinear stiffness mechanisms. Appl Math Mech 2022;43(7):1081–108. http://dx.doi.org/10.1007/S10483-022-2864-6.
[45] Chen S, Guo B, Said HA, Yang K, Ringwood JV. Wave-to-wire modelling of a vibro-impact wave energy converter for ocean data buoys. IFAC-PapersOnLine 2023;56(2):11735–40. http://dx.doi.org/10.1016/J.IFACOL.2023.10.543.
[46] Xu X, Wiercigroch M. Approximate analytical solutions for oscillatory and rotational motion of a parametric pendulum. Nonlinear Dynam 2007;47(1–3):311–20. http://dx.doi.org/10.1007/S11071-006-9074-4.
[47] Yurchenko D, Alevras P. Dynamics of the N-pendulum and its application to a wave energy converter concept. Int J Dyn Control 2013;1(4):290–9. http://dx.doi.org/10.1007/S40435-013-0033-X.
[48] Najdecka A, Vaziri V, Wiercigroch M. Synchronization control of parametric pendulums for wave energy extraction. Renew Energy Power Qual J 2011;1(9):535–9. http://dx.doi.org/10.24084/REPQJ09.383.
[49] De Paula AS, Savi MA, Wiercigroch M, Pavlovskaia E. Bifurcation control of a parametric pendulum. Int J Bifurcation Chaos 2012;22(5). http://dx.doi.org/10.1142/S0218127412501118.
[50] Yurchenko D, Alevras P. Parametric pendulum based wave energy converter. Mech Syst Signal Process 2018;99:504–15. http://dx.doi.org/10.1016/j.ymssp.2017.06.026.
[51] Zhou X, Zhang H, Jin H, Liu C, Xu D. Numerical and experimental investigation of a hinged wave energy converter with negative stiffness mechanism. Int J Mech Sci 2023;245:108103. http://dx.doi.org/10.1016/j.ijmecsci.2023.108103.
[52] Zhang H, Zhang J, Zhou X, Shi Q, Xu D, Sun Z, et al. Robust performance improvement of a raft-type wave energy converter using a nonlinear stiffness mechanism. Int J Mech Sci 2021;211:106776. http://dx.doi.org/10.1016/j.ijmecsci.2021.106776.
[53] Gomes RPF, Henriques JC, Gato LM, Falcao AFdO. Experimental tests of a 1:16th scale model of the spar-buoy owc in a large scale wave flume in regular waves. 2018, p. 1–10.
[54] Payne GS, Taylor JR, Bruce T, Parkin P. Assessment of boundary-element method for modelling a free-floating sloped wave energy device. Part 2: Experimental validation. Ocean Eng 2008;35(3–4):342–57. http://dx.doi.org/10.1016/J.OCEANENG.2007.10.008.
[55] Cordonnier J, Gorintin F, De Cagny A, Clément AH, Babarit A. SEAREV: Case study of the development of a wave energy converter. Renew Energy 2015;80:40–52. http://dx.doi.org/10.1016/J.RENENE.2015.01.061.

[56] Kurniawan A, Grassow M, Ferri F. Numerical modelling and wave tank testing of a self-reacting two-body wave energy device. Ships Offshore Struct 2019;14(sup1):344–56. http://dx.doi.org/10.1080/17445302.2019.1595924.
[57] Orszaghova J, Wolgamot H, Draper S, Eatock Taylor R, Taylor PH, Rafiee A. Transverse motion instability of a submerged moored buoy. Proc R Soc Lond Ser A Math Phys Eng Sci 2019;475(2221). http://dx.doi.org/10.1098/rspa.2018.0459.
[58] Lelkes J, Davidson J, Kalmár-Nagy T. Modelling of parametric resonance for heaving buoys with position-Varying Waterplane Area. J Mar Sci Eng 2021;9(11):1162. http://dx.doi.org/10.3390/JMSE9111162.
[59] Olvera A, Prado E, Czitrom S. Parametric resonance in an oscillating water column. J Engrg Math 2007;57(1):1–21. http://dx.doi.org/10.1007/s10665-006-9048-z.
[60] Ding R, Zhang H, Xu D, Liu C, Shi Q, Liu J, et al. Experimental and numerical study on motion instability of modular floating structures. Nonlinear Dynam 2023;111(7):6239–59. http://dx.doi.org/10.1007/s11071-022-08163-2.
[61] Giorgi G. Embedding parametric resonance in a 2:1 wave energy converter to get a broader bandwidth. Renew Energy 2024;222:119928. http://dx.doi.org/10.1016/J.RENENE.2023.119928.
[62] Giorgi G, Sirigu S, Bonfanti M, Bracco G, Mattiazzo G. Fast nonlinear Froude–Krylov force calculation for prismatic floating platforms: A wave energy conversion application case. J Ocean Eng Mar Energy 2021;7(4):439–57. http://dx.doi.org/10.1007/s40722-021-00212-z.
[63] Habib G, Giorgi G, Davidson J. Coexisting attractors in floating body dynamics undergoing parametric resonance. Acta Mech 2022;233(6):2351–67. http://dx.doi.org/10.1007/S00707-022-03225-3.
[64] Nallayarasu S, Mathai TP. Effect of mathieu instability on motion response of spar hull with heave damping plate. Ships Offshore Struct 2016;11(8):833–46. http://dx.doi.org/10.1080/17445302.2015.1073866.
[65] Aziminia MM, Abazari A, Behzad M, Hayatdavoodi M. Stability analysis of parametric resonance in spar-buoy based on Floquet theory. Ocean Eng 2022;266:113090. http://dx.doi.org/10.1016/J.OCEANENG.2022.113090.
[66] Shi B, Yang J, Wiercigroch M. Vibrational energy transfer in coupled mechanical systems with nonlinear joints. Int J Mech Sci 2023;260:108612. http://dx.doi.org/10.1016/J.IJMECSCI.2023.108612.
[67] Gomes R, Henriques J, Gato L, Falcão A. Time-domain simulation of a slack-moored floating oscillating water column and validation with physical model tests. Renew Energy 2020;149:165–80. http://dx.doi.org/10.1016/J.RENENE.2019.11.159.
[68] Niosi F, Begovic E, Bertorello C, Rinauro B, Sannino G, Bonfanti M, et al. Experimental validation of orcaflex-based numerical models for the PEWEC device. Ocean Eng 2023;281:114963. http://dx.doi.org/10.1016/J.OCEANENG.2023.114963.
[69] Al Shami E, Wang X, Ji X. A study of the effects of increasing the degrees of freedom of a point-absorber wave energy converter on its harvesting performance. Mech Syst Signal Process 2019;133:106281. http://dx.doi.org/10.1016/j.ymssp.2019.106281.
[70] Budal K, Falnes J. Wave power conversion by point absorbers: A norwegian project. Int J Ambient Energy 1982;3(2):59–67. http://dx.doi.org/10.1080/01430750.1982.9675829.
[71] Wang H, Zhu S. Latching control: A wave energy converter inspired vibration control strategy. Mech Syst Signal Process 2024;208:110912. http://dx.doi.org/10.1016/j.ymssp.2023.110912.
[72] Gioia DG, Pasta E, Brandimarte P, Mattiazzo G. Data-driven control of a pendulum wave energy converter: A Gaussian process regression approach. Ocean Eng 2022;253:111191. http://dx.doi.org/10.1016/J.OCEANENG.2022.111191.
[73] Fontana M, Casalone P, Sirigu S, Giorgi G, Bracco G, Mattiazzo G. Viscous damping identification for a wave energy converter using CFD-URANS simulations. J Mar Sci Eng 2020;8(5). http://dx.doi.org/10.3390/JMSE8050355.
[74] Perez T, Fossen TI. Time- vs. Frequency-domain identification of parametric radiation force models for marine structures at zero speed. Modelling Identif Control 2008.
[75] Penalba M, Ringwood JV. A high-fidelity wave-to-wire model for wave energy converters. Renew Energy 2019;134:367–78. http://dx.doi.org/10.1016/j.renene.2018.11.040.
[76] Giorgi G, Ringwood J. Analytical formulation of nonlinear Froude–Krylov forces for surging-heaving-pitching point absorbers. In: Proceedings of the international conference on offshore mechanics and arctic engineering, vol. 10. 2018, http://dx.doi.org/10.1115/OMAE2018-77072.
[77] Giorgi G. Nonlinear Froude–Krylov Matlab demonstration toolbox. 2019, http://dx.doi.org/10.5281/zenodo.4682671.
[78] Clément AH, Ferrant P. Superharmonic waves generated by the large amplitude heaving motion of a submerged body. In: Nonlinear water waves: IUTAM symposium, Tokyo Japan, August 25–28, 1987. Berlin, Heidelberg: Springer Berlin Heidelberg; 1988.
[79] Colón D. Balthazar J, Marcelo Tusset A, Yassin H, Demonte Gonzalez T, Parker G, et al. Effect of the dynamic Froude–Krylov force on energy extraction from a point absorber wave energy converter with an hourglass-shaped buoy. Appl Sci 2023;13(7):4316. http://dx.doi.org/10.3390/APP13074316.
[80] Giorgi G, Ringwood JV. Nonlinear Froude–Krylov and viscous drag representations for wave energy converters in the computation/fidelity continuum. Ocean Eng 2017;141(June):164–75. http://dx.doi.org/10.1016/j.oceaneng.2017.06.030.
[81] Giorgi G, Gomes RP, Henriques JC, Gato LM, Bracco G, Mattiazzo G. Detecting parametric resonance in a floating oscillating water column device for wave energy conversion: Numerical simulations and validation with physical model tests. Appl Energy 2020;276. http://dx.doi.org/10.1016/j.apenergy.2020.115421.
[82] Rodríguez CA, Neves MA, Polo JCF. A time-efficient approach for nonlinear hydrostatic and Froude–Krylov forces for parametric roll assessment in irregular seas. Ocean Eng 2016;120:246–55. http://dx.doi.org/10.1016/J.OCEANENG.2016.04.020.
[83] Leary M, Rusch C, Zhang Z, Robertson B. Comparison and validation of hydrodynamic theories for wave energy converter modelling. Energies 2021;14(13):3959. http://dx.doi.org/10.3390/EN14133959.
[84] Kurniawan A, Tran TT, Brown SA, Eskilsson C, Orszaghova J, Greaves D. Numerical simulation of parametric resonance in point absorbers using a simplified model. IET Renew Power Gener 2021;15(14):3186–205. http://dx.doi.org/10.1049/RPG2.12229.
[85] Mérigaud A, Ringwood JV. Free-surface time-series generation for wave energy applications. IEEE J Ocean Eng 2018;43(1):19–35. http://dx.doi.org/10.1109/JOE.2017.2691199.
[86] Rajarathinam M, Awrejcewicz J, Ali SF. Energy generation through a hybrid energy harvester under random excitation. Int J Mech Sci 2024;273:109187. http://dx.doi.org/10.1016/J.IJMECSCI.2024.109187.
[87] Najdecka A, Narayanan S, Wiercigroch M. Rotary motion of the parametric and planar pendulum under stochastic wave excitation. Int J Non-Linear Mech 2015;71:30–8. http://dx.doi.org/10.1016/J.IJNONLINMEC.2014.12.008.
[88] Hasselmann K, Barnett TP, Bouws E, Carlson H, Cartwright DE, Enke K, et al. Measurements of wind-wave growth and swell decay during the joint north sea wave project. Tech. Rep., JONSWAP, Hamburg: Deutsches Hydrographisches Institut; 1973.
[89] Boashash B. Estimating and interpreting the instantaneous frequency of a signal—Part 1: Fundamentals. Proc IEEE 1992;80(4):520–38. http://dx.doi.org/10.1109/5.135376.
[90] Welch PD. The use of fast Fourier transform for the estimation of power spectra: A method based on time averaging over short, modified periodograms. IEEE Trans Audio Electroacoust 1967;15(2):4.